Journal of Hydrology 184 (1996) 57-84

Journal of Hydrology

Radar mapping of surface soil moisture

Fawwaz T. Ulaby[a,*], Pascale C. Dubois[b], Jakob van Zyl[b]

[a]Electrical Engineering and Computer Science, University of Michigan, Ann Arbor, MI 48109-2122, USA

[b]Jet Propulsion Laboratory, Pasadena, CA 911(11-8099, USA

California Institute of Technology,

Received 7 June 1995; accepted 29 October 1995

Abstract

Intended as an overview aimed at potential users of remotely sensed spatial distributions and temporal variations of soil moisture, this paper begins with an introductory section on the fundamentals of radar imaging and associated attributes. To place the soil moisture sensing task in proper perspective, (he prerequisite step of classifying terrain into four basic types---bare surfaces, short vegetation, tall vegetation, and urban - is addressed by demonstrating howadual-frequency polarimetric radar can correctly classify terrain with an accuracy greater than 90%. Over S000 image pixels with known terrain identity were involved in the evaluation of the radar image classifier. For bare soil (with vegetation cover shorter than 15 cm), radar can estimate the volumetric moisture content (expressed in per cent) of the top 5 cm soil layer with an r.m.s. error of 3.5%. Based on theoretical model predictions as well as experimental observations, strong evidence exists in support of radar's potential for sensing soil moisture under vegetation cover, but no operational algorithm exists at present.

1. Imaging radar over-view

High-resolution imaging radar systems operate in a side-tooking mode as illustrated in Fig. 1. The imaging radar configuration most commonly used today is the synthetic aperture radar (SAR) which transmits a series of pulses as the radar antenna flies across the imaged scene, and then these pulses arc processed together to simulate a very long aperture capable of very high angular resolution along the direction of flight (Ulaby et al., 1982; Elachi, 1988; Curlander and McDonough, 1991). The along-flight direction is usually called the azimuth direction and the direction across the imaged swath is called the ground-range direction. The

* Corresponding author

0022-1694/96/$ 15.00
SSDI 0022 -1694(95)02968-0

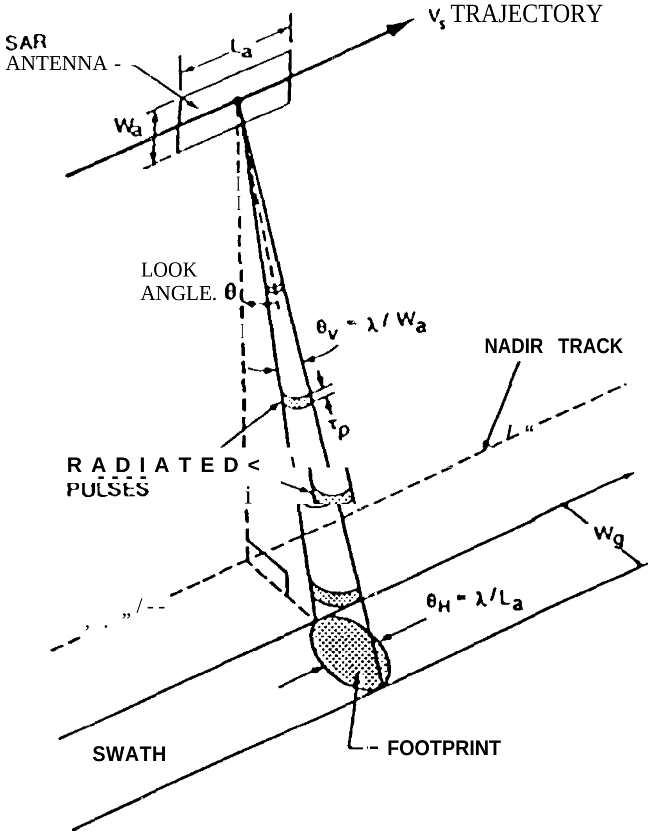

Fig. 1. Radar imaging geometry L_a, antenna length; W_a, antenna width; W_g, swathwidth; τ_p, pulse length; θ, incidence angle

resolving capability of an SAR along the ground-range direction is realized by transmitting very short pulses. For a pulse of length τ_p, the ground-range resolution is:

$$r_g = \frac{c\tau_p}{2\sin\theta} \tag{1}$$

where c is the velocity of light and θ is the incidence angle. Because of the sin θ dependence, SAR systems are seldom used to image the ground surface at angles smaller than 15°. In the azimuth direction, the ultimate resolution of an SAR is

$$r_a = L_a/2 \tag{2}$$

when L_a is the antenna length,

The purpose of this section is to present an overview of the operational characteristics of an SAR system and to relate the quantities measured by the radar to the scattering parameters of the imaged scene. To focus the discussion on spaceborne SARs in particular, we shall often use the Shuttle Imaging Radar-C (SIR-C) for

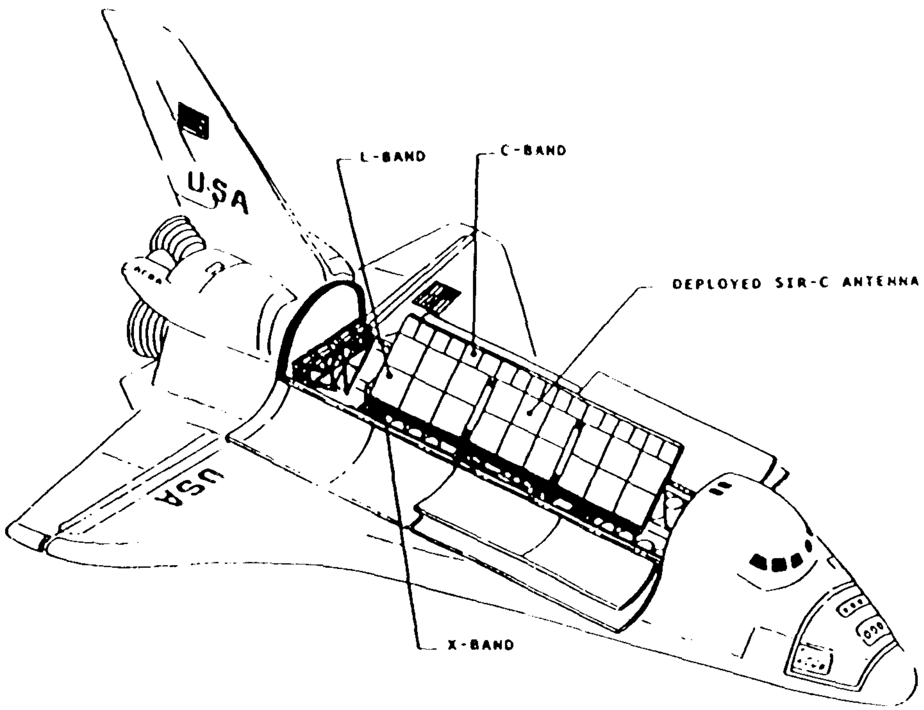

Fig. 2 Deployed antenna in the Shuttle Payload Bay

illustration purposes (Fig. 2). SIR-C, which flew on the Space Shuttle in April and October 1994, is a joint US–European design consisting of two polarimetric SARs operating at L-band (23.5 cm wavelength) and C-band (5.8 cm wavelength), both designed and built by the Jet Propulsion Laboratory (JPL), and a single polarization SAR operating at X-band (3.1 cm wavelength), built by a joint German-Italian consortium. Table 1 provides a summary of the SIR-C- X-SAR system characteristics (Jordan et al., 1991).

1.1. Single-look vs. multi-look resolution

The single-look resolution of an SAR system refers to the resolving capability that

Table 1
SIR-C–X-SAR system characteristics

Parameter	L-Band	C-Band	X-Band
Orbital altitude (km)	225	225	225
Wavelength (m)	0,235	0058	0.031
Resolution (m)	-30 x 30	-30 x 30	-30X30
Swathwidth (km)	15-90	15 90	1540
Look angle range (from nadir)	17–63°	17 63°	17-63°

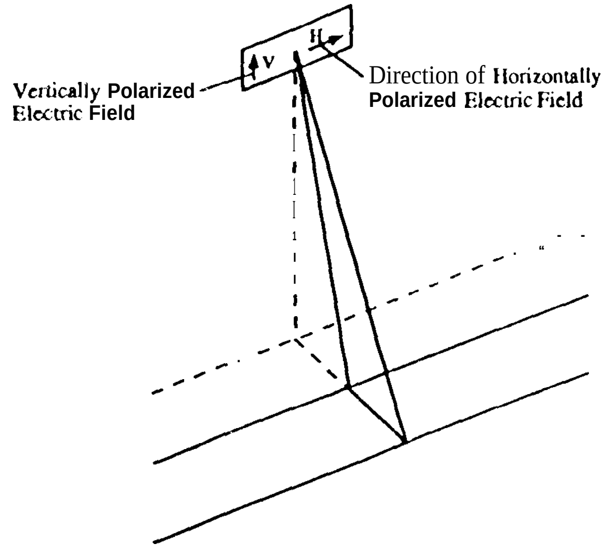

Fig. 3. A dual-polarized radar antenna has two sets of elements, one for transmitting (or receiving) waves with horizontally polarized electric fields and the other for vertically polarized electric fields.

can be provided by an SAR, given its antenna length, pulse length (or bandwidth) and incidence angle. Corresponding to SIR-C'S 12 m long antenna and 20 MHz bandwidth, the single-look resolutions arc r_a = 6 m and r_g = 15 m at an incidence angle θ = 30°. Single-look images arc not used in practice for interpretation purposes because such images arc noisy in appearance owing to the coherent nature of the imaging process (Ulaby et al., 1986). 10 reduce tbc noise, or image speckle, the resolution is degraded by averaging several pixels together. Typically, several pixels arc averaged along the azimuth dimension of the image, as well as along the range dimension if necessary, to produce an image with pixels having approximately square dimensions and representing, [he average of several looks. For SIR-C–X-SAR, this multi-look resolution is of the order of 30 m x 30 m. Thus, to a user of SAR imagery, this multi-look resolution is a more meaningful measure of the resolution capability of tbc system. Single-look images arc used for special purposes, such as system performance evaluations and calibration experiments.

1.2. *Polarization*

Wave polarization refers to the direction of the electric field of the electromagnetic wave transmitted or received by a radar antenna. For a horizontally polarized antenna, its elements are configured to transmit or receive waves whose electric field points only along the length of the antenna (Fig. 3), which is also parallel to the Earth's surface. The electric field direction for a vertically polarized antenna is along its height dimension, as illustrated in Fig. 3. Because the process by which radar waves are scattered by terrain surfaces and volumes (such as vegetation) is a function of the polarization of the incident wave, radars use multiple polarizations to image terrain, to increase the amount of information extractable from radar images. If the incident wave is horizontally polarized, the energy backscattered towards the radar will, in general, consist of a wave that is also horizontally polarized, as well as a wave that is vertically polarized. The latter is referred to as cross-polarized.

A polarimetric radar, such as the L-band and C-band SARS of SIR-C, is capable of measuring the radar response for VV, HH, HV, and VH, where the first letter denotes the polarization of the receive antenna and the second letter denotes the polarization of the transmit antenna. Because of a reciprocity property of radar scattering, the responses for HV and VH are identical. The quantity measured by the radar is called a scattering matrix, which later is converted to the scattering coefficient σ° (Ulaby and Elachi, 1990). The scattering coefficient, which is a unitless quantity representing the radar cross-section (in m^2) of a given pixel on the ground per unit (physical) area of that pixel (in m^2), is akin to the optical reflectivity responsible for the intensity recorded by an optical imaging system. To denote the receive–transmit polarization combination associated with the scattering coefficient, the latter is denoted by σ_{ij}°, where i,j = H or V. Often, because σ_{ij}° may exhibit a wide dynamic range, it is expressed in decibels:

$$\sigma_{ij}^\circ\,(\mathrm{dB}) = 10\log\sigma_{ij}^\circ\,(\mathrm{m^2\,m^{-2}}) \tag{3}$$

In addition to measuring σ_{hh}°, σ_{vv}°, and σ_{hv}°, which collectively are referred to as the multi-polarized magnitudes of the scattering response, a polarimetric radar can measure the polarization phase differences between the multi-polarized backscattered waves: co-polarized phase difference:

$$\phi_c = \phi_{hh} - \phi_{vv} \tag{4}$$

cross-polarized phase difference:

$$\phi_x = \phi_{hv} - \phi_{vv} \tag{5}$$

In practice, ϕ_x has not been found to contain much useful information about the imaged scene. In contrast, the co-polarized phase difference ϕ_c has proved to be a very useful parameter in image classification.

In summary, a polarimetric radar is capable of producing five basic products of the imaged scene, namely three images representing the magnitudes σ_{hh}°, σ_{vv}°, and σ_{hv}°, and two images representing ϕ_c and ϕ_x. All five co-registered images are manifestations of the scattering character of the scene, and are independent of all system parameters except for the wavelength λ and the incidence angle θ at which the scene is imaged.

1.3. Swathwidth

SIR-C was designed to generate images with swathwidths varying between 15 km and 90 km, depending on the specific mode selected for imaging. The different modes

Table 2
SAR frequency bands in the 0.2–15 GHz Range

Letter designation	frequency (GHz)	Wavelength (cm)	Space SARS
P-Band	0.44	68	
L-Band	1.28	23	Seasat, SIR-A, SIR-B, J-ERS-1, SIR-C
S-band	3.0	20	Almaz-1
C-Band	5.3	5.7	ERS-1, SIR-C, Radarsat
X-Band	9.6	3.1	SIR-C

correspond to different combinations of bands, polarizations, and spatial resolution. The constraint is imposed by the data rate allowable by the TDRS communication channel. Conceptually, it is possible to image the terrain with a 30 m spatial resolution over a swath several hundred kilometers in width. This can be achieved by increasing the TDRS data rate, or by partial preprocessing of the SAR data on board before transmission At this stage, SIR-C is regarded as an experimental system providing the opportunity to evaluate the use of space SAR data for a variety of oceanographic, geologic, hydrologic, and ecological applications.

1.4. *Microwave band*

SAR systems are designed to operate at specific frequencies (wavelengths) designated by the Federal Communication Commission as allowable bands for radar transmission. Table 2 provides a summary of these bands for the commonly used part of the microwave frequency range, together with the commonly used letter designations.

The choice of bands for remote sensing is dictated by two sets of factors: (1) technology considerations, such as the availability of space-qualified power sources to provide the necessary transmitter power; (2) the dependence of the scattering by and propagation through terrestrial media on wavelength. Further discussion of the role of wavelength relative to the soil-moisture sensing problem is given in Section 3.

2. Image classification

Section 3 and Section 4 of this paper discuss the status of algorithms used to estimate soil moisture content from the measured radar response for bare-soil surfaces and vegetation-covered surfaces, respectively. Before the application of such algorithms, however, it is necessary to classify the imaged scene with as much detail as possible. Numerous techniques have been proposed for classifying terrain on the basis of SAR images (Wu and Sader, 1987; Kong et al., 1987; Yueh et at., 1988; Lim et al., 1989; Lin and Allebach, 1990; Rignot and Chellappa, 1992; Van Zyl and Burnette, 1992; Lozano-Garcia and Hoffer, 1993; Wong and Posner, 1993). In this section, we describe the capability of an SAR image classifier that was developed at the University of Michigan in support of the SIR-C April 1994 mission, as well as the JPL AIRSAR, which is an airborne version of SIR-C. Actually, the classifier is part of an image interpretation processor designed to

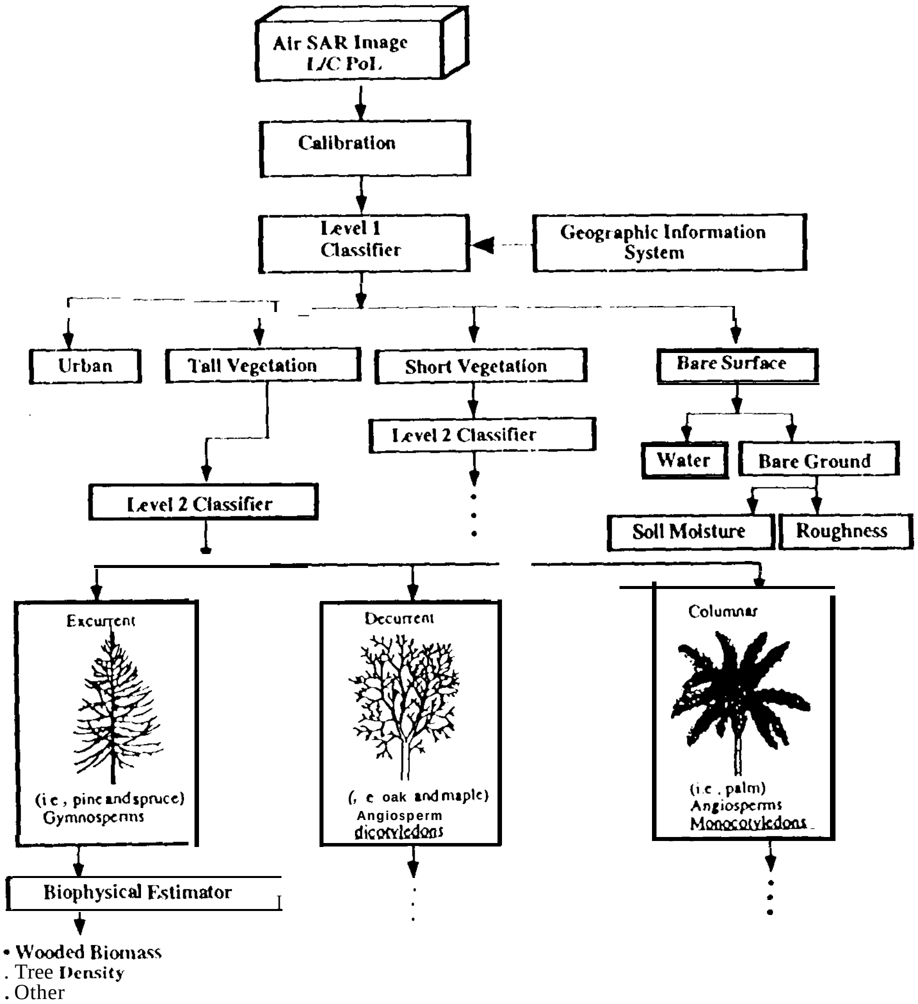

Fig. 4. Block diagram for the SAR Image Interpretation Processor developed at the University of Michigan.

extract various types of terrain data from the L-band and C-band polarimetric radar data (Dobson et al., 1995; Pierce et al., 1994). A diagram of the image interpretation processor is shown in Fig. 4. After calibrating the SAR images (using techniques that were developed over the past 5 years at JPL and the University of Michigan), a Level-1 classifier is applied to classify each pixel in the imaged scene as urban, tall vegetation (trees), short vegetation (grasses and crops), or bare surface. Bare surfaces include water surfaces, roads, and bare soil surfaces with vegetation cover less than 15 cm in height. A summary of the operation of the Level-1 classifier and its identification accuracy is given in Section 2.1.

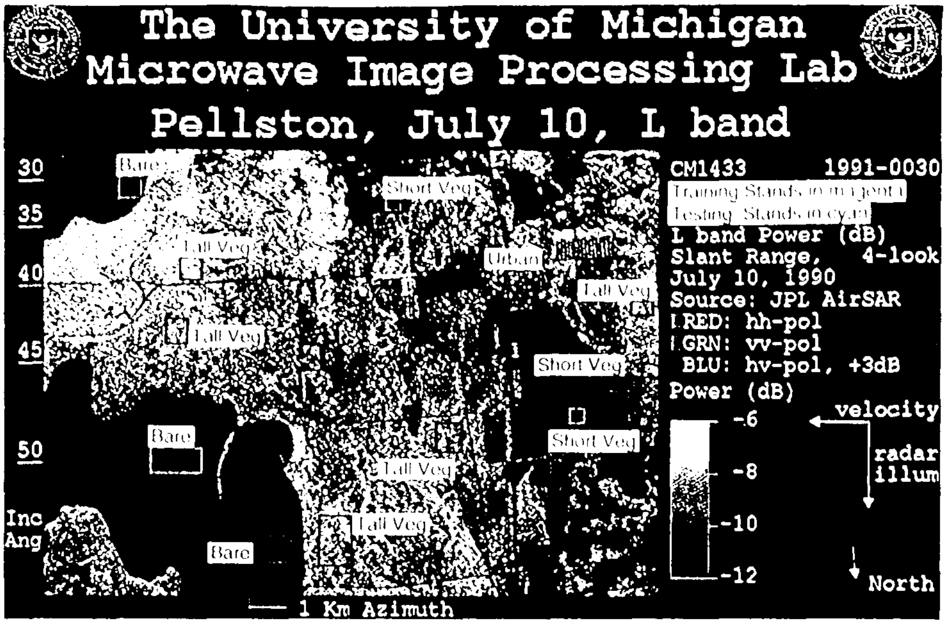

Fig. 5. L-Band SAR image of the Pellston area in northern Michigan. The image was acquired by the JPL AIRSAR system.

For the non-water-covered bare surfaces, the algorithm described in Section 3 is used to estimate the soil moisture content and the roughness of the soil surface, as shown in Fig. 4. For the tall vegetation and short vegetation pixels, a Level 2 classifier is applied to each, to further refine the identity of the vegetation cover. Tree canopies, for example, are classified as excurrent (e.g. pine and spruce), decurrent (e.g. oak and maple), or columnar (e.g. palm). This classification scheme is based on the canopy structural character as viewed by a radar wave. Finally, for each canopy class, a biophysical estimator is used to estimate such parameters as total above-ground biomass and tree density (number of trees per unit area), as described by Dobson et al. (1995).

5.1. Terrain classifier

Fig. 5 is an SAR image of an area located in northern Michigan. The image, which was acquired by the JPL AIRSAR system on 10 July 1991, covers an area 7.5 km × 12.4 km, represented by 750 × 1024 pixels, each 6.6 m × 12 m in area. A comprehensive geographic information data base in available for the imaged area, including digital terrain elevation, soil type, and ground cover. Specific areas (identified by square boxes on the image in Fig. 5) were selected for evaluating the classification accuracy of the classifier. Fig. 6 shows the sequential steps used by the classifier. Each step identifies the specific radar parameters used in that step. For example, the tall-vegetation step uses $\sigma_{hh}^{0}(L)$ and $\sigma_{hv}^{0}(L)$, which are the measured HH- and HV-polarized backscattering coefficients at L-band. These two parameters are capable of identifying tall vegetation correctly (Fig. 7) with

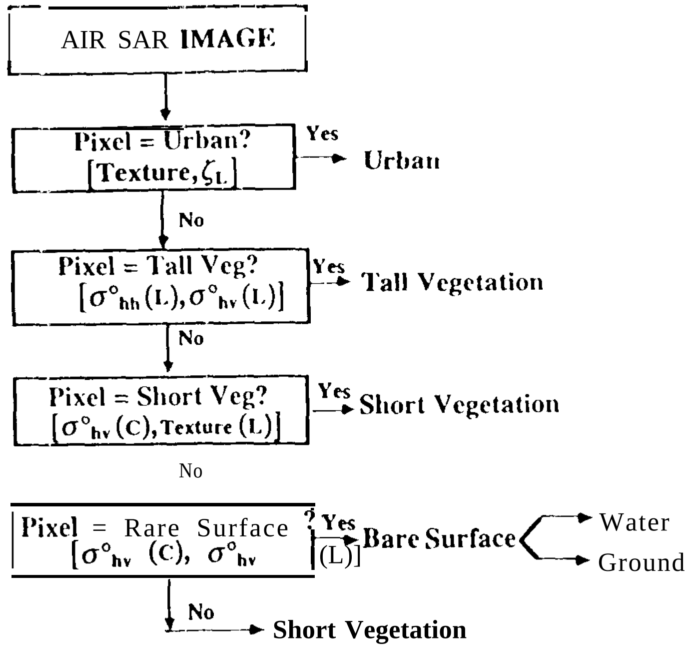

Fig. 6. Level-1 sequential classifier. The quantifies in square brackets inside the boxes refer to the measured SAR image parameters used in that step. Texture is related to image speckle

an accuracy of 98%. Comparable results are obtained for the short-vegetation and bare-surface classes (Table 3), but not for urban pixels. The classification accuracy for urban pixels is only 30% because although the geographic information data base would identify an area as urban, in reality that area may contain vegetation and other types of cover; therefore, it is not possible for the radar to classify it as urban, Table 3 contains classification results obtained by the same classifier when applied to two different test sites, imaged 3 months apart. In each study, over 5000 image pixels with known terrain identity (established by direct ground observations) were involved in evaluating the accuracies given in Table 3.

3. Radar estimation of bare-soil attributes

The magnitude of the backscattering coefficient σ° of a ground surface observed by a radar system is governed by two quantities: (a) the dielectric constant of the ground surface; (b) the roughness of the surface. The dielectric constant is, in turn, very strongly dependent on the moisture content of the soil surface layer, and to a much *lesser* extent, on the soil textural composition and physical temperature (for non-frozen soil). Accordingly, this section deals with three topics: (1) the relationship

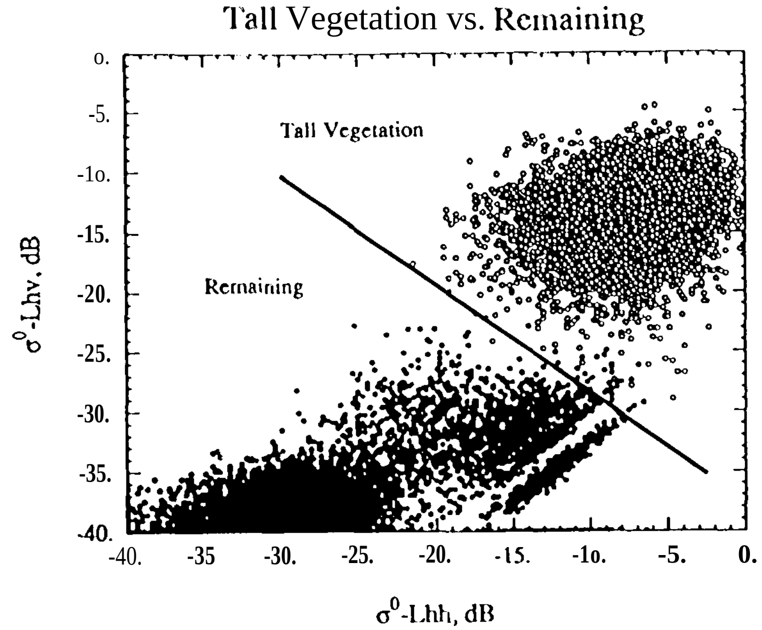

Fig. 7. Scatterogram for two SAR parameters, $\sigma_{hv}^{\circ}(L)$ and $\sigma_{hh}^{\circ}(L)$, used for separating tall vegetation pixels from all others with an accuracy of 98%

between the dielectric constant of a soil medium and its physical properties; (2) the depth of penetration associated with a microwave propagating in a soil medium; (3) the algorithm used for estimating the soil's moisture content from the observed radar response.

Table 3
Classification results for two areas imaged 3 months apart; no urban areas were present in the Raco area

Classified as	True class			
	Urban	Tall vegetation	Short vegetation	Bare surface
Pellston, MI				
Urban	30.7	0.22	0	0.06
Tall vegetation	37.9	98.32	0	0
Short vegetation	28.5	1.46	94.74	0.87
Bare surface	2.9	0	5.26	99.07
Raco, MI				
Urban		0	0	0
Tall vegetation		100	0	0
Short vegetation	-	0	99.12	2,06
Bare surface		0	0.88	97.94

3.1. Soil dielectric properties

The dielectric constant ϵ of a material, which is a fundamental properly that characterizes both the reflection and attenuation properties of a wave interacting with that material, consists of a real part ϵ' and an imaginary part ϵ'':

$$\epsilon = \epsilon' - j\epsilon'' \tag{6}$$

The dielectric constant ϵ is related to the index of refraction of the material, n, by

$$n = \sqrt{\epsilon} \tag{7}$$

The index of refraction also is a complex quantity composed of a real part n' and an imaginary part n'':

$$n = n' - jn'' \tag{8}$$

and these two parts arc related to ϵ' and ϵ'' by

$$n' = \mathrm{Re}\{\sqrt{\epsilon}\} \tag{9}$$

$$n'' = |\mathrm{Im}\{\sqrt{\epsilon}\}| \tag{10}$$

and the inverse relationships arc given by

$$\epsilon' = (n')^2 - (n'')^2 \tag{11}$$

$$\epsilon'' = 2n'n'' \tag{12}$$

Fora homogeneous soil medium with a flat surface, the reflectivity for nadir incidence is given try

$$\Gamma = \left|\frac{n-1}{n+1}\right|^2 = \left|\frac{\sqrt{\epsilon}-1}{\sqrt{\epsilon}+1}\right|^2 \tag{13}$$

The reflectivity Γ determines the fraction of the power incident upon the surface that is reflected back by the surface, and the transmissivity T determines the fraction transmitted across the air–soil boundary into the soil medium. Conservation of power requires that

$$T = 1 - \Gamma \tag{14}$$

For incidence at angles other than normal incidence, the incidence angle θ also is involved, as is the polarization of the wave. If the soil surface is not perfectly smooth, the incident power is scattered in many directions, including the backscatter direction (Fig. 8). The component scattered in the backscatter direction provides the link between the power received by the radar and the properties of the soil medium.

The power transmitted into the soil medium decays exponentially at a rate governed by the attenuation coefficient of the soil medium, α, which is related to n and ϵ by

$$\alpha = \frac{2\pi}{\lambda} n'' = \frac{2\pi}{\lambda}|\mathrm{Im}\{\sqrt{\epsilon}\}| \tag{15}$$

If ϵ of the soil medium is not constant with depth, then both Γ and α arc governed by the depth profile of ϵ for the layer between the surface and approximately δ_p, where δ_p is the

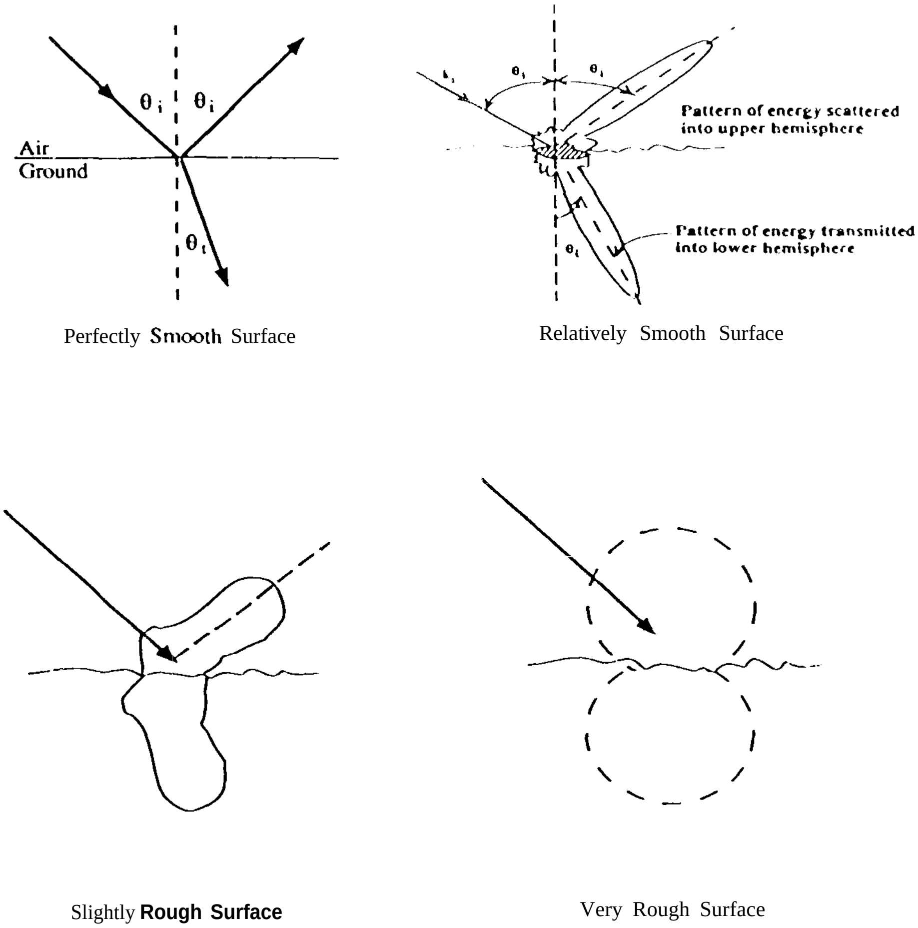

Fig. 8. The angular distribution of energy scattered by a surface depends on its roughness

penetration depth of the soil medium. For a homogeneous soil medium,

$$\delta_p = \frac{1}{2\alpha} \tag{16}$$

The preceding material provided the basic relationships between the soil dielectric constant ϵ and the reflectivity Γ, attenuation coefficient α and penetration depth δ_p. Now we shall examine the dependence of ϵ on the soil's physical properties. This dependence is also a function of the microwave frequency f. To avoid overcomplicating the. picture, however, we shall limit most of the discussion to the L-band region $f \approx 1$ GHz), which is qualitatively representative of the entire frequency range usually considered for soil moisture sensing (0.4--10 GHz).

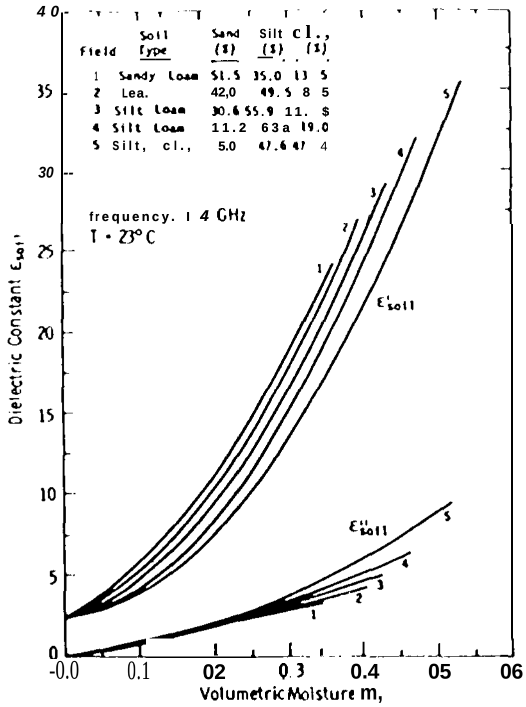

Fig. 9. Measured dielectric constant for five soils at 1.4 GHz (Ulaby et al., 1986)

For oven-dried soil, the real part ϵ' varies between 2 and 4 (depending on the soil bulk density ρ_b), and is essentially independent of both temperature and frequency. The imaginary part, ϵ'', is typically less than 0.05. In contrast, the dielectric constant of water at 1 GHz at room temperature is ϵ' -80 and ϵ'' - 4. Consequently, the addition of water to soil causes the dielectric constant of the mixture to increase, with the increase being governed by the volume fraction of the mixture composed of water. Fig. 9 shows plots of ϵ' and ϵ'' as a function of the volumetric water content m_v for five soil types. In all cases, both ϵ' and ϵ'' exhibit strong variations with m_v, and relatively weak sensitivities to soil type. Also, for m_v > 0.05, the soil bulk density ρ_b dots not influence ϵ, as long as the water content is expressed on a volumetric basis.

Unless it changes phase into ice, water exhibits a relatively weak dependence on temperature. Hence, the soil–water mixture also is insensitive to physical temperature for 7'> 0°C. A large change, however, takes place as the soil freezes, as indicated by the curves in Fig. 10.

3.2. *Penetration depth*

The plots shown in Fig. 11 depict the variation of the penetration depth δ_p with volumetric moisture content m_v at three microwave frequencies for a homogeneous loamy soil. At L-band (1.3 GHz), the depth decreases from I m at m_v = 1% down to 6 cm at 40%. As

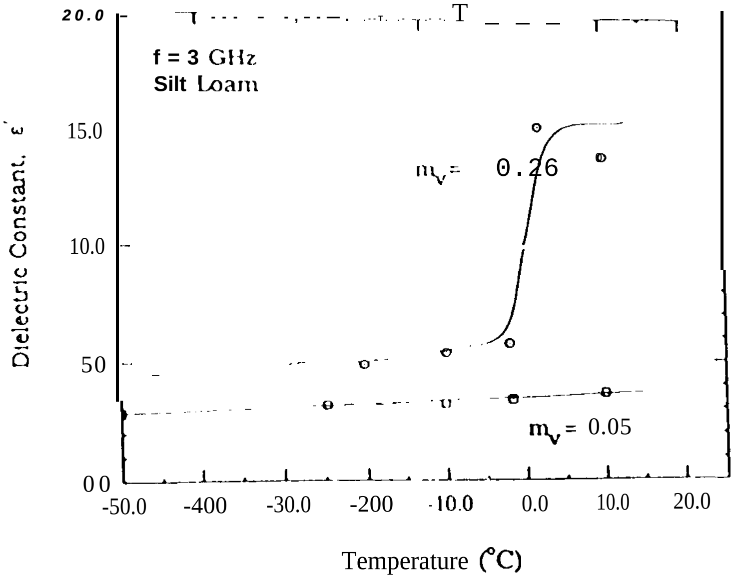

(a) Real Part ε′

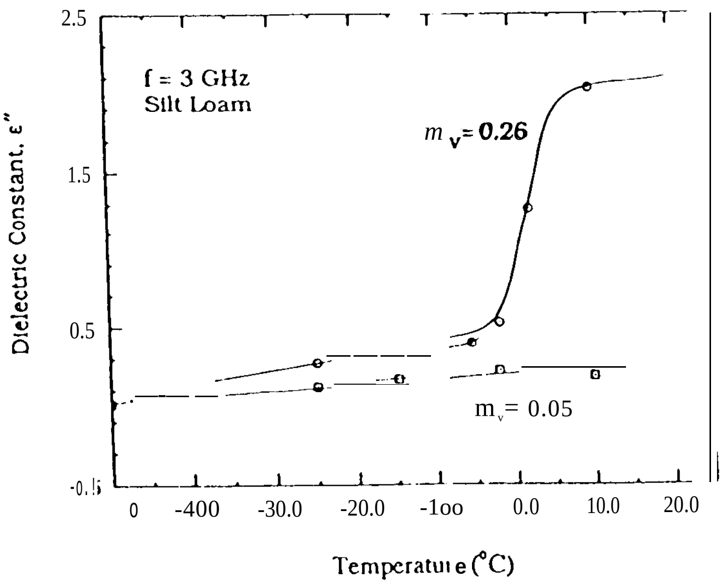

(b) Imaginary Part ε″

Fig. 10. Temperature dependence of soil dielectric constant at two moisture contents

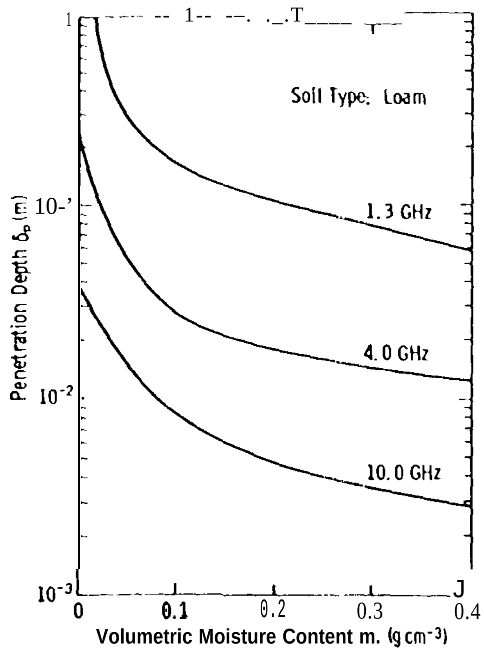

Fig. 11. Penetration depth as a function of *moisture* content for loamy soil at three microwave frequencies

mentioned above, the penetration depth is a measure of the thickness of the top surface layer of the soil medium governing the backscatter observed by a radar system (or the emission in the case of passive microwave sensing). It dots not follow, however, that the penetration depth is equal to the thickness of the soil layer whose moisture is measured by the radar. This is because not only is the near-surface soil moisture important, but so is the depth profile of the moisture content over the extent of the penetration depth. As a first-order approximation, wc find in practice that the thickness of the layer whose moisture is estimated by I,-band radar is of the order of 5 cm.

3.3. Radar algorithm for measuring soil moisture content

Because the soil dielectric constant exhibits a strong response to moisture content, so dots the backscattering coefficient o". Fig. 12 depicts the variation of σ° with m_v for two soil surfaces with different roughnesses, where roughness is represented by the standard deviation of surface height s (also called r.m.s. height). If the surface roughness remains approximately constant or varies over a narrow range, it is possible to usc radar to monitor the change in moisture content, as a function of time for example, but it is difficult to measure m_v on an absolute scale. In the general case, it is necessary to usc a multi-channel radar to measure both s and m_v. This can be done by using a single-frequency multi-polarization system capable of measuring all three linear polarization components of u", namely σ_{hh}°, σ_{vv}°, and σ_{hv}°.

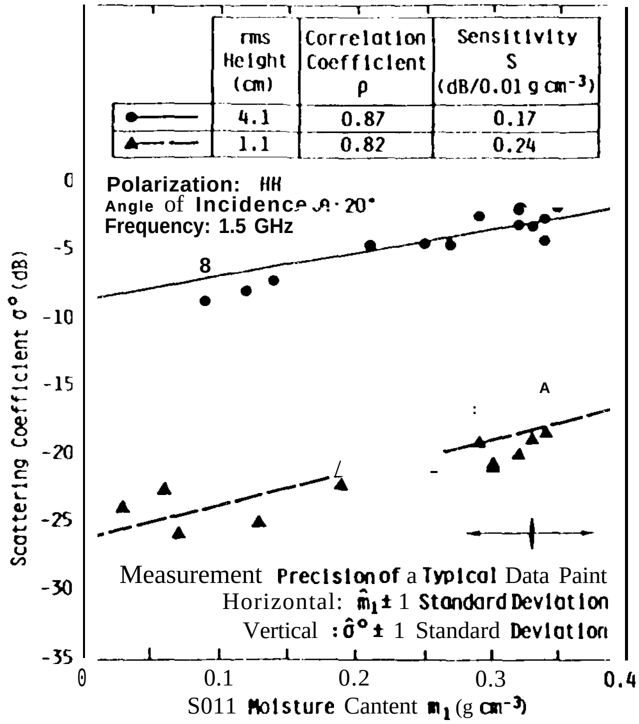

Fig. 12 Comparison of the backscattering response to m_l of a smooth surface and a rough surface for $\theta = 20°$ at $f = 1.5$ GHz (Ulaby et al, 1986)

The algorithm given in Fig. 13 uses two radar-derived parameters as input—(a) $p = \sigma_{hh}^\circ/\sigma_{vv}^\circ$, the co-polarized ratio; (b) $q = \sigma_{hv}^\circ/\sigma_{vv}^\circ$, the cross-polarized ratio—and provides the roughness parameters and volumetric moisture content m_v as output (Oh et al., 1992). This algorithm is based on a model and extensive experimental data measured at L-band. The moisture content m_v represents the average moisture content of the top 5 cm layer. The performance of the soil-moisture estimation algorithm is shown in Fig. 14, where radar-derived estimates of s and m_v are compared with corresponding values measured in situ.

Although this technique was derived for bare-soil surfaces, it is equally applicable to soil surfaces with modest vegetation cover. If the vegetation is less than 10–15 cm in height, the presence of the vegetation cover imparts a minor effect on the radar response of the underlying soil surface at low microwave frequencies (such as L-band). For dense or tall vegetation cover, it is necessary either to modify the estimation algorithm by accounting for the attenuation and scattering effects of the vegetation, which would require the availability of independent information about the vegetation structure and biomass, or to use a different algorithm that utilizes multi-frequency radar observations. This topic is discussed in the next section.

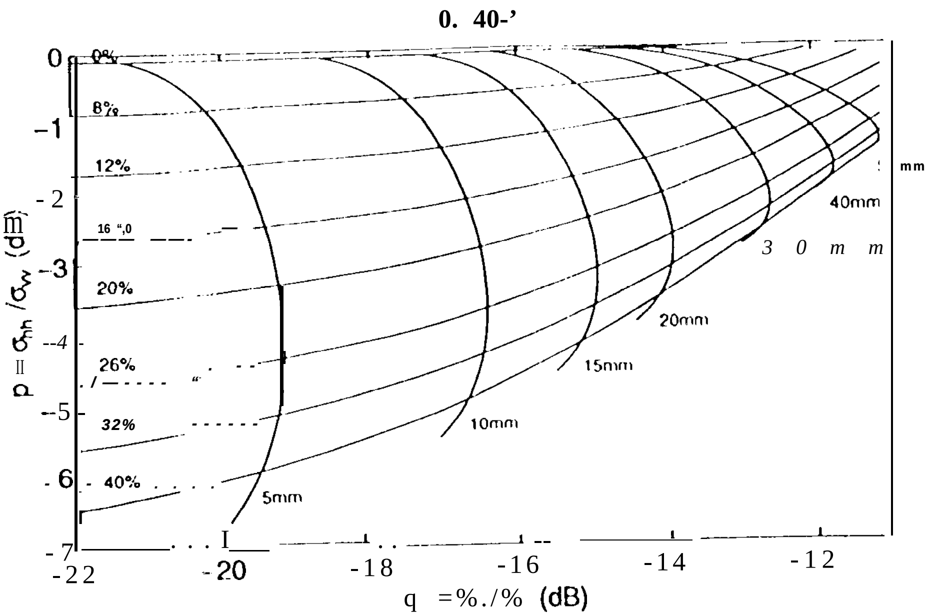

Fig. 13. Soil-moisture SAR estimation algorithm for bare-soil surfaces at L-band (1.25 GHz) and incidence angle θ of 40°. The two sets of curves denote different values of m_v (in per cent) and the r.m.s. height s (in mm)

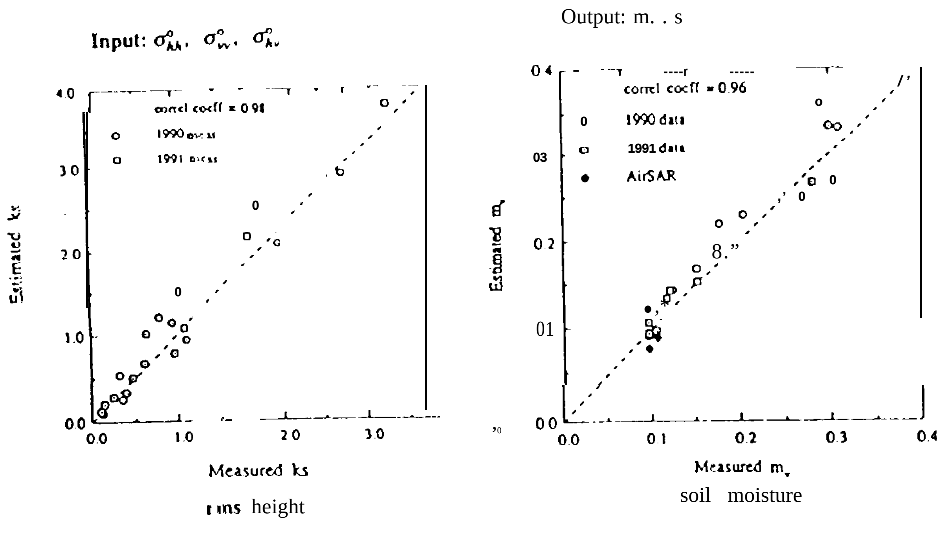

Fig. 14. Comparison of radar-estimated surface roughness and moisture content with in situ measurements.

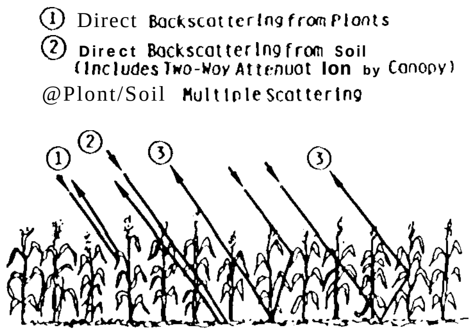

Fig. 15 Backscattering contributions of a canopy over a soil surface

4. Effects of vegetation cover

The radar backscatter for a vegetation-covcrcd soil surface consists of three types of contributions:

$$\sigma^\circ = T^2\sigma_s^\circ + \sigma_{dv}^\circ + \sigma_{int}^\circ \tag{17}$$

where σ°_s is the backscatter contribution of the (bare) soil surface, T^2 is the two-way attenuation of tbc vegetation layer, σ_{dv}^0 is the direct backscatter contribution of the vegetation layer, and σ_{int}° represents multiple scattering involving the vegetation elements and the ground surface. These mechanisms arc illustrated diagrammatically in Fig. 15. For vegetation with above-ground biomass less than 0.5 kg m^{-2}, $T^2 \approx 1$ and the second and third terms in Eq. (17) arc negligibly small, and therefore the effect of the vegetation cover may be ignored. In the general case, σ^0 is governed by the soil properties (roughness and moisture content) as well as the structure and biomass of the vegetation cover,

The vegetation-related quantities depend on the radar wave parameters: the wavelength λ, polarization configurations of the transmit and receive antennas, and the incidence angle θ, and on the vegetation geometry and dielectric properties. As with soil, the dielectric constant of vegetation is strongly influenced by the moisture content. Vegetation geometry includes both the macrostructure of a vegetation canopy, such as the height of the canopy and the number of plants or trees per unit area, and tbc microstructure, which refers to the stalks and leaves. For well-cbaractcrized canopies, it is possible to usc electromagnetic scattering models to compute the radar backscattering coefficient σ° and its constituent components, as given in Eq. (17), for any radar wavelength, polarization configuration and incidence angle. These models arc highly complex, owing primarily to the complex nature of the vegetation scattering medium, and therefore it is not possible to describe them in any adequate detail in this paper. Instead, wc will examine the effects of vegetation cover from the standpoint of sensing soil moisture through a combination of model calculations and experimental observations. The model calculations arc based on the MIMICS code (Michigan Microwave Canopy Scattering Model), which is a vector radiative transfer formulation that accounts for single scattering mechanisms involving single

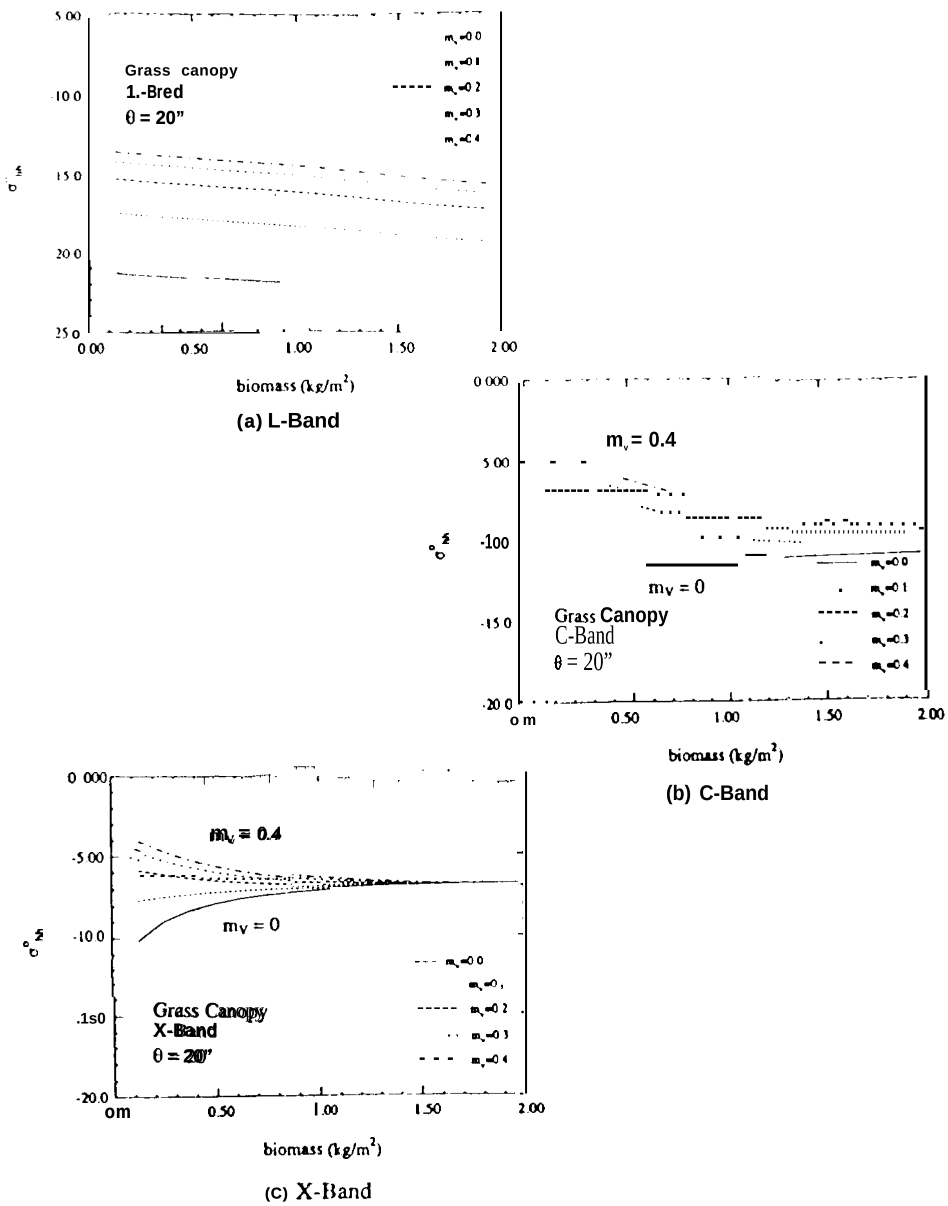

Fig. 16. Backscatter variation with biomass for a grass canopy.

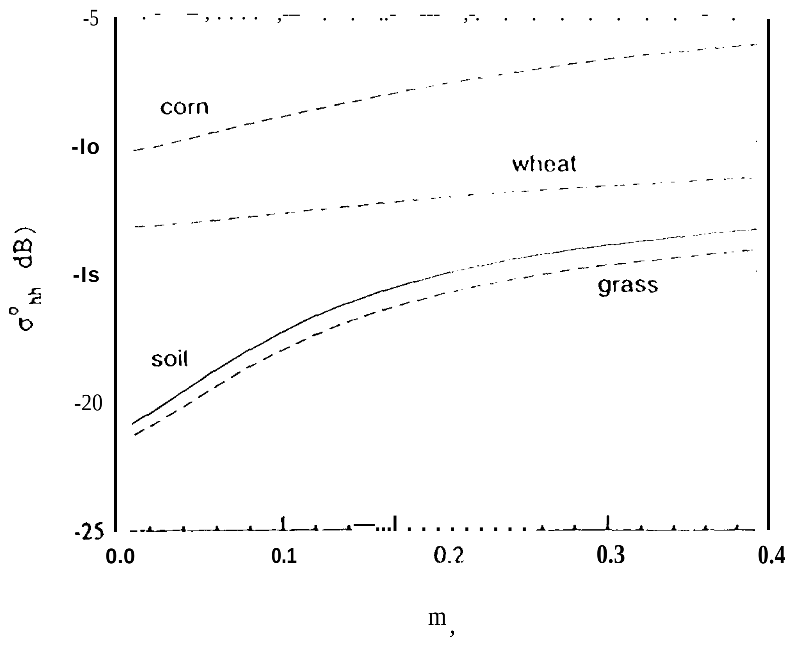

Fig. 17. L-Band backscatter response to soil moisture content at 20° incidence for bare soil and three vegetation canopies: grass (height 1 m, LAI 7, dry biomass 1.3 kg m^{-2}, leaf density 25 000 m^{-3}, leaf moisture content 0.8), wheat (height 1 m, LAI 2.2, stem density 500 m^{-3}, leaf density 2500 m^{-3}, leaf moisture content 0.8), and corn (height 25 m, LAI 4.56, dry biomass 1.84 kg m^{-2}, moisture content 0.8). The canopy parameters are based on field data for mature vegetation.

interaction between the vegetation elements and the underlying soil surfaces (Ulaby et al., 1990).

4.1. *Backscatter response*

Fig. 16 depicts the variation of σ° with biomass for a layer of grass above a soil surface, for each of several soil moisture conditions, and Fig. 17 shows the soil moisture response of σ° for three. types of vegetation cover. For each vegetation cover, the vegetation parameters were selected to represent fully mature conditions, and therefore the most difficult from the standpoint of wave penetration through the vegetation layer. The plots given in Fig, 16 and Fig. 17 arc based on model calculations performed using the MIMICS code. It is clear from these figures that to measure soil moisture content with radar, it is necessary to have information about the vegetation cover. A possible approach for obtaining this information is to use a multi-frequency radar system that can simultaneously estimate both the soil and vegetation parameters of interest, Different frequencies exhibit different transmissivities through a vegetation canopy (as illustrated by Fig. 18) as well as different scattering responses.

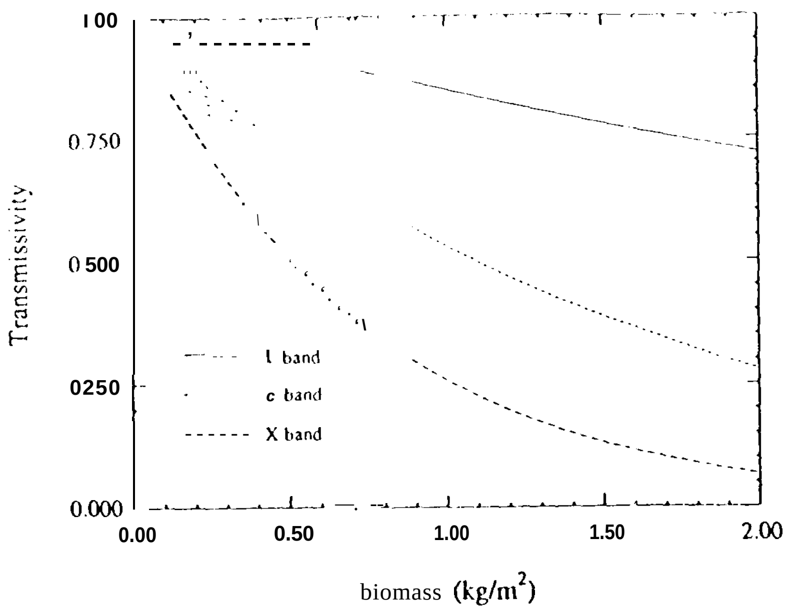

Fig. 18. Canopy transmissivity for HH polarization at 20° for a grass canopy

4.2. Experimental observations

Extensive experimental evidence supports the conclusion that radar waves can penetrate through vegetation, particularly in the Iongcr-wavelength segment of the microwave band (λ >5 cm). Two examples arc provided in Fig. 19 and Fig. 20, with the former showing measured values of σ° as a function of soil moisture content for fields planted in soybeans and mile, and the latter showing similar plots based on SIR-B measurements for various types of cover. individually, for each of the vegetation covers, σ° exhibits a good response torn,; however, the response curves have different slopes and intercepts, again pointing out the need to determine the vegetation parameters in conjunction with the soil sensing problem. This may be accomplished through the usc of n]ulti-frequency multi-polarization observations to simultaneously estimate both the soil and vegetation-cover parameters governing the radar backscatter. Such an approach is being pursued by both the University of Michigan and JPL.

S. Soil moisture maps from AIRSAR and SIR-C

In 1992, the JPL AIRSAR system was flown on eight different days from 10 June to 18 June over the Little Washita watershed in southwestern Oklahoma. The SAR observations, which were part of a major NASA-supported hydrology field investigation known as the Washita '92 Experiment, were made from a nominal flight altitude of 7.9 km. This section

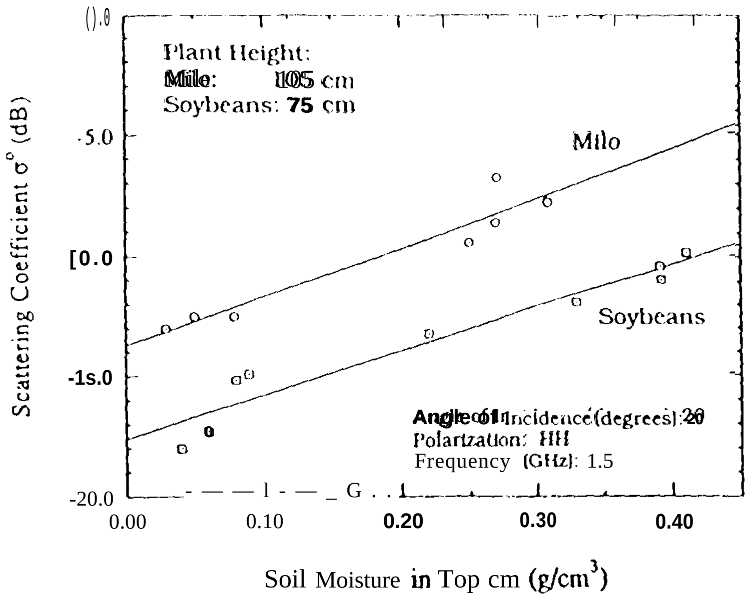

Fig. 19. Measured backscatter response for milo and soybeans.

provides a brief description of the SAR system, followed by a presentation of multi-date soil moisture maps generated on the basis of the radar images. Only a cursory description of the Washita test site is given in this paper, as it has already been well characterized in the paper by Jackson and Le Vine (1996).

5.1. AIRSAR instrument

The AIRSAR instrument is a fully polarimetric multifrequency SAR system mounted onboard a DC-8 aircraft operated by NASA-Ames (Van Zyl et al., 1992). The radar acquires data on the left of the nadir track as the aircraft flies at an average velocity of 420 knots. It measures the full scattering matrix by transmitting alternately H- and V-polarized waves and receiving with two antennas of perpendicular polarization orientations. It operates at C-band (5.7 cm), L-band (24 cm) and P-band (68 cm) simultaneously, producing three sets of overlapping data.

The recorded raw data return must be processed on the ground into SAR imagery. The standard processed frame size (for 20 MHz data) is 12 km in the along-track direction by 8.5 km in the across-track direction with a pixel size of 6.6 m x 12.1 m in the across-track and along-track directions, respectively. The calibration of the data is performed in the processor by using both the calibration parameters derived for the flight campaign and routine system tests. Fifteen trihedral corner reflectors, each measuring 2.4 m on a side, are deployed on the Rosamond dry lake bed in California to cover the full radar swath. The calibration site is imaged at the beginning of the radar campaign and calibration parameters are derived matching the radar cross-section of the trihedral reflector to its

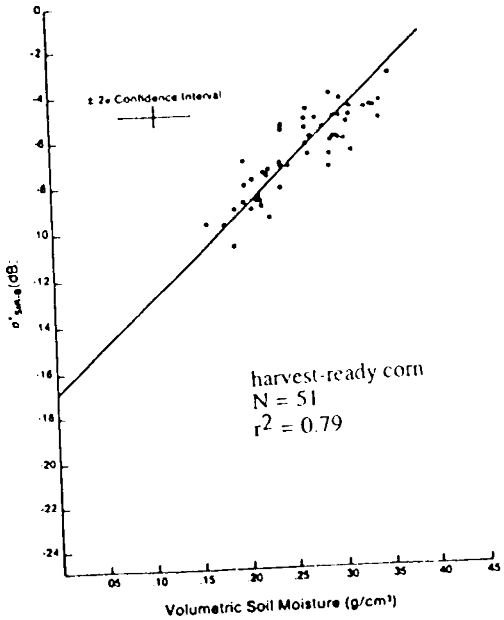

(a) Corn

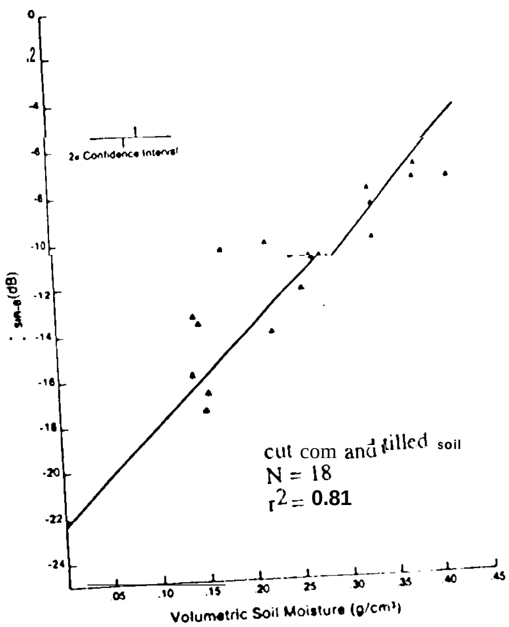

(b) Cut corn and tilled bare soil

Fig. 20. Radar response to soil moisture, as measured by the Shuttle Imaging Radar-B in 1984: (a) harvest-ready corn; (b) cut corn and tilled bare soil. (From Dobson and Ulaby (1986).)

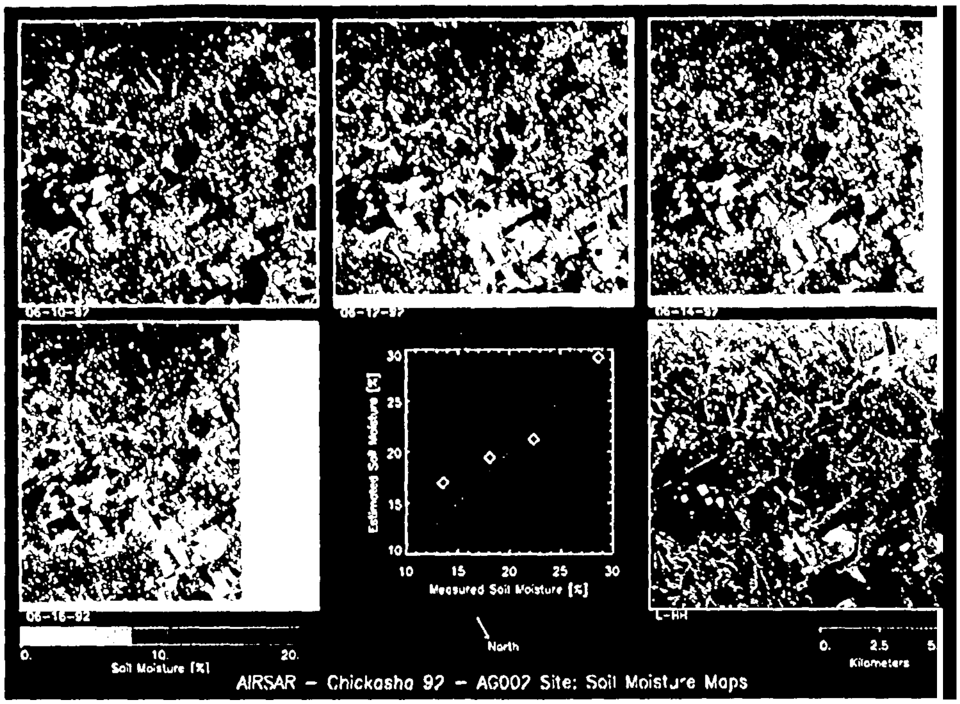

[illegible] theoretical [illegible]. The accuracy of the AIRSAR [illegible] is estimated to be within a few [illegible].

[illegible] Washita '92 AIRSAR campaign

[illegible] Washita '92 AIRSAR [illegible] SAR [illegible] of the whole watershed. During data acquisition the radar system produces [illegible] band image of the scene. This product is available in the aircraft and [illegible] used to evaluate the quality of the data and to detect anomalous effects. Throughout the watershed, field boundaries are generally oriented north–south and east–west, and in many cases metal fences are used to mark the field boundaries. The [illegible] images acquired on the test flight led to the decision to tilt the flight lines away from the east heading to avoid the strong radar returns from the fences running east–west.

The AIRSAR processor is configured to produce images 12.8 km × 8 km in area. The black and white image shown in Fig. [illegible] is such an example. The four colour images are estimated soil moisture maps for 10, 12, 14 and 16 June, all generated by applying a soil moisture inversion algorithm to the multi-polarization L-band images. The algorithm used is very similar to the one discussed above [illegible] and [illegible] L-band to infer surface roughness and soil moisture (Dubois [illegible]). The 10 June image corresponds to very wet conditions owing to extensive [illegible] that occurred during the preceding

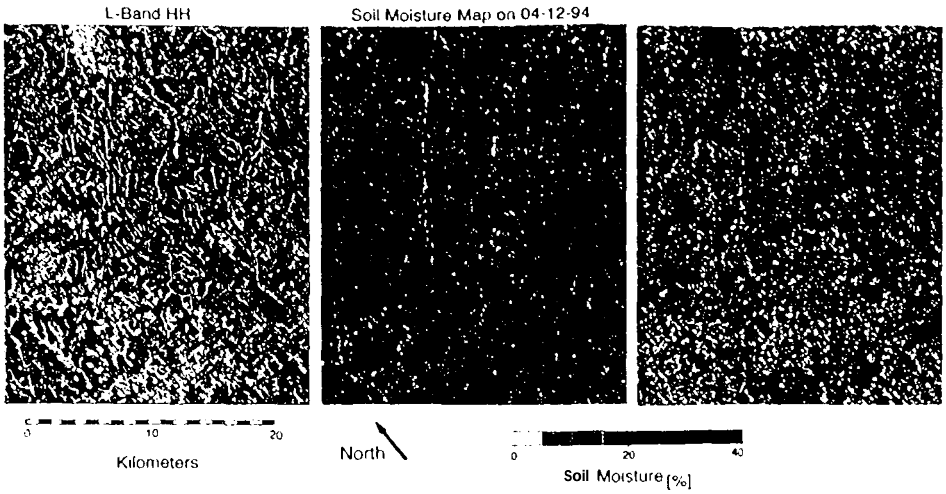

Fig. 22. L-Band hh-polarized image and two soil moisture maps derived from SIR-C data for 12 and 15 April 1994. The first day was extremely wet and the second day was drier.

2 weeks. No additional precipitation occurred between 10 June and the final flight on 18 June, leading to continuous dry-down between those two dates. This dry-down pattern is clearly reflected in the soil-moisture estimated maps shown in Fig. 21, with the 10 June map being predominantly dark blue, denoting high moisture content, and the maps corresponding to succeeding dates exhibiting progressively larger segments that are yellow, denoting low moisture states. These results are particularly significant in view of the fact

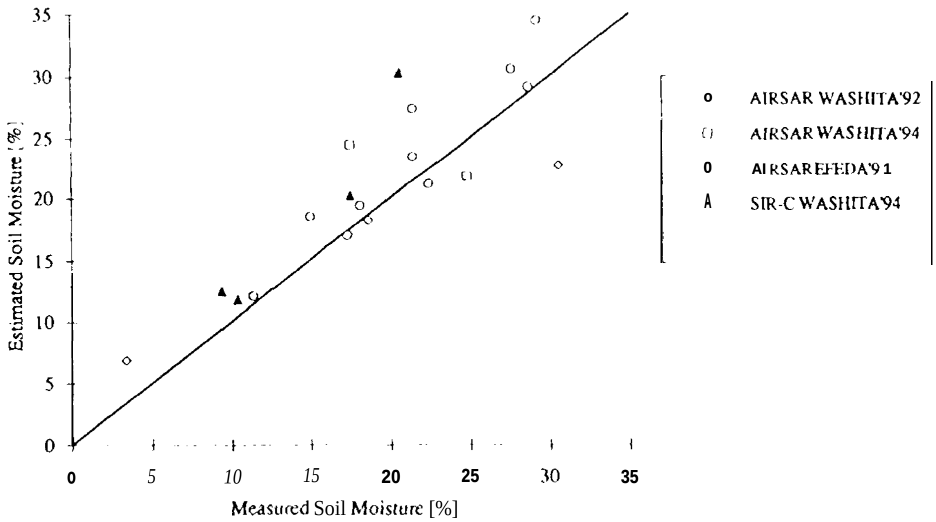

Fig. 23. Comparison of radar-estimated soil moisture values for bare-soil fields with in situ measurements. The SAR observations were extracted from several AIRSAR campaigns and from SIR-C overpasses in April 1994.

that the moisture maps were generated by an algorithm that had been developed on the basis of radar measurements for bare-soil surfaces, with no attempt made to correct or account for vegetation cover (detailed land-use and soil-type maps arc available in the paper by Jackson and Le Vine, 1996). Scattering from vegetation will result in a higher $\sigma_{hh}^{\circ}/\sigma_{vv}^{\circ}$ ratio than scattering from a bare surface alone. This will cause the algorithm to underestimate soil moisture over the vegetated field, The effect can be seen in the 10 June map, where the areas in yellow (dry) correspond to the more heavily vegetated surfaces, Fig. 21 includes a typical example of a quantitative comparison between the in situ measurements of soil moisture for onc of the bare-soil fields and the corresponding values estimated by the radar algorithm.

5.3. *SIR-C SAR observations*

During its April 1994 mission, the SIR-C instrument aboard the Space Shuttle acquired SAR imagery of the Washita test site on 1 t- 17 April. Fig. 22 shows an L-band single-polarization image of a 25 km x 25 km area, and soil moisture maps for 12 and 15 April. The soil moisture maps were generated by applying the same SAR algorithm as described above in conjunction with Fig. 21. The average soil moisture over the site was estimated to be in the neighborhood of 20% on 12 April, compared with only 10% on 15 April. This is because no rain had occurred over this time period. The significant change in moisture is reflected in the color change towards yellow between the two moisture maps.

Fig. 23 provides a summary of the quantitative analysis derived from both the AIRSAR and SIR-C SAR observations over the Washita test site. Comparison of soil moisture values estimated using the SAR inversion algorithm with their field counterparts based on direct in situ measurements reveals good agreement between them. With volumetric soil moisture expressed in pcr cent, correlation analysis indicated that the overall r.m.s. error is 3.5%.

The results of the Washita 1992 AIRSAR and 1994 SIR-C SAR campaigns, which arc based on onty I.-band observations, arc strong testimony to radar's potential as a soil moisture mapper. Current research aims to usc both 1.- and C-band observations to simultaneously estimate both soil moisture and vegetation biomass of vegetation-covcrcd areas, thereby providing more accurate soil moisture maps over a wide range of cover conditions.

6. **Concluding remarks**

The highlights of this overview presentation are as follows:

1. the combination of L- and C-band polar imetric SAR observations can provide Level-1 terrain classification accuracies of the order 90% or better for tall vegetation (trees), short vegetation (grasses and crops), and bare surfaces (water, roads, and bare soil).
2. For bare-soil surfaces, multi-polarization I.-band observations can be used to estimat

the soil moisture content of the top 5 cm layer and the surface roughness with a high degree of accuracy. The estimation algorithm is equally applicable for vegetation-covered surfaces if the vegetation height is less than 15 cm.

3. For vegetation-covered surfaces, the radar response is governed by both the soil and vegetation parameters. Strong evidence exists to suggest that it should be possible to develop a radar algorithm for estimating soil moisture in the presence of vegetation cover. Such an algorithm is currently under development.

References

Curlander, J.C. and McDonough, R N., 1991. Synthetic Aperture Radar Systems and Signal Processing. Wiley. New York

Dobson, M C. and Ulaby, F.T. 1986 Preliminary evaluation of the SIR-B response to soil moisture, surface roughness, and crop canopy cover. IEEE Trans. Geosci Remote Sensing, GE-24(4) 517-526.

Dobson, M. C., Ulaby, F. T'. and Pierce, L.E., 1995. Land-cover classification and estimation of terrain attributes using Synthetic Aperture Radar. Remote Sensing Environ , 1S1.S('[' Special Issue, S1: 19%214.

Dubois, P. C., van Zyl, J. and Engman, T., 1995. Measuring soil moisture with imaging radars. IEEE Trans Geosci. Remote Sesing, 33:915--926.

Elachi, C., 1988. Spaceborne Radar Remote Sensing: Applications and Techniques. IEEE Press, New York

Jackson, T.J. and Le Vine, D.E., 1996. Mapping surface soil moisture using an aircraft-based passive microwave instrument: algorithm and example. J. Hydrol., 184: 85-99.

Jordan, R L., Huneycutt, B.L. and Werner, M , 1991. The SIR-C/X-SAR Synthetic Aperture Radar System IEEE Proc., 79(6): pp. 827-83S

Kong, J.A , Schwartz, A.A , Yueh, H.A., Novak, L. M. and Shin, R 1., 1987. Identification of terrain cover using the optimum polarimetric classifier. J. Electromagn Wave Appl , 2(2) 171

[im, H }1., Schwartz, A. A., Yueh, H.A , Kong, J. A., Shin, R T. and van Zyl, J. J., 1989. Classification of earth terrain, using polarimetric synthetic aperture radar images J Geophys Res 94(116) 7049.

[in, Q. and Allebach, J.E'., 1990. Combating speckle in SAR images vector filtering and sequential classification based on a multiplicative noise model. IEEE Trans Geosci Remote Sensing, 28(4) 634.

Lozano-Garcia, D.F. and Hoffer, R M., 1993. Synergistic effects of combined Landsat-TM and SIR-B data for forest resources assessment. Int J. Remote Sensing, 14. 26-77

oh, Y., Sarabandi, K and Ulaby, F'.'J'., 1992. An empirical model and an inversion technique for radar scattering from bare soil surfaces IEEE Trans. Geosci Remote Sensing, 30 37(I- 382

Pierce, 1. E , Ulaby, F.T., Sarabandi, K and Dobson, M C , 1994. Knowledge-based classification of polarimetric SAR images IEEE Trans. Geoscience Remote Sensing, 32: 1081-1086

Rignot, E and Chellappa, R., 1992. Segmentation of polarimetric synthetic aperture radar data IEEE Trans. Image Proc., 1:281-300

Ulaby, F.T. and Elachi, C. (Editors), 1990. Radar Polarimetry for Geoscience Applications Artech House, Norwood, MA.

Ulaby, F.T., Moore, M.K. and Fung, A K., 1982. Microwave Remote Sensing, Active and Passive, Vol 2 Artech House, Norwood, MA

Ulaby, F.T., Moore, M.K. and Fung, A.K , 1986. Microwave Remote Sensing, Active and Passive, Vol 3. Artech House, Norwood, MA.

Ulaby, F.T'., Sarabandi, K., McDonald, K., Whitt, M. and Dobson, M (' , 1990. Michigan Microwave Canopy Scattering Model (MIMICS). Int. J. Remote Sensing, 11(7) 1223-1253.

Van Zyl, J.J. and Burnette, C.F'., 1992. Bayesian classification of polarimetric SAR images using adaptive a priori probabilities Int J. Remote Sensing, 13(5): 835.

Van Zyl, J. J., Carande, R., Lou, Y., Miller, T. and Wheeler, K , 1992 The NASA/JPL Three Frequency Polarimetric AIRSAR System. IGARSS '92 Proceedings IEEE, Houston, pp. 649 650

Wong, Y.-F. and Posner, E C., 1993. A new clustering algorithm applicable to multispectral and polarimetric

,/ ' , / ' ,' 'f. i'. '